Surface profile of material ablated with high-power lasers in ambient air medium

Vatsya, S.R.; Li, C.; Nikumb, S.K.

Publisher's version / Version de l'éditeur:
https://doi.org/10.1063/1.1846141
Journal of Applied Physics, 97, 3, 2005

Surface profile of material ablated with high-power lasers in ambient air medium

S. R. Vatsya, C. Li and S.K. Nikumb

Integrated Manufacturing Technologies Institute

National Research Council of Canada

800 Collip Circle, London, ON, Canada, N6G 4X8

Abstract

In general, material processing with high power ultra-short-pulsed lasers yields cleaner surfaces, as long as the intensity profile of the laser beam is well shaped. However, the beam suffers distortions during propagation through ambient atmospheric mediums such as air. Passage through such mediums causes the beam to self-focus increasing the intensity further and causing the breakdown of the gas. The resulting plasma distorts the beam's original profile and the ablated surface conforms to the beam profile. A numerical scheme is developed here to calculate the intensity profile of an optical beam propagating through a medium. Intensity distribution of the beam is then used to determine the profile of the processed surface by a geometrical method developed recently. The calculated profile is compared with the experimentally obtained surface with good agreement. For medium spot sizes, the self-focusing and plasma effects tend to cancel each other, maintaining the intensity profile of the beam similar to the original Gaussian distribution. For small spot sizes when the intensity is high, the plasma effects are found to distort the beam profile. This indicates that the experimental parameters can be adjusted to improve the quality of the machined surface.

PACS Numbers: 02.60.Lj, 41.85.Ew, 42.65.Jx.

I. INTRODUCTION

High power densities and minimal heat-affected zone are major factors associated with ultrashort-pulsed laser processing, which are responsible for improving the quality of the fabricated features, textures, without changes in the bulk properties. For these reasons, femtosecond laser processing of materials is preferred over the lasers with longer pulse widths.[1,2] Processes have been developed that enable machining of features significantly smaller than the diffraction limit, i.e. sub-micron features inside transparent bulk materials[3] and nanoscale features on the surface of thin metal films[4], by taking an advantage of the threshold effect[5].

With rapid development of compact, stable regeneratively amplified Ti:Sapphire lasers in recent years, applications of high power femtosecond lasers in industrial sector are increasing. However, nonlinear wavefront distortion due to the optical breakdown of surrounding atmosphere by extremely high intensity of the focused femtosecond laser beam creates a major obstacle. The Kerr effect describing self-focusing of the beam increases the already high intensity, which causes the breakdown of air. Processes involved in the generation of plasma and its subsequent interaction with the beam, diffuse and distort the beam profile, at times offsetting some of the advantages. In addition, deflection of the s-polarized radiation at the hole wall makes its shape irregular.[6] Since these effects, which result in poor feature quality of the machined work piece, are created or magnified by the passage of the optical beam through dielectric material, e.g., air, machining is normally conducted in vacuum, which restricts its application in the production environment[7]. Among others[8], use of inert gases as media for beam delivery has been suggested for these reasons, e.g., helium, because of its high ionization potential[9,10], but the inconvenience persists.

Since the profile of the fabricated surface conforms to that of the optical beam, there is considerable interest in calculating the beam shape propagating through dielectric media, which is described by a nonlinear Schrodinger type equation[9,11,12]. This equation is usually solved by the fast Fourier transform[9] and the finite difference[11,12] methods. In the present article, we develop a new scheme taking advantage of the fact that the closed form solutions for propagation in vacuum are available[13]. This enables an isolation of the perturbing effects, which tend to cancel each other over a significant intensity range. Therefore, more accurate solutions are expected to result. Consequent representation of the solution also suggests a natural grid structure in the radial coordinate varying in proportion to the beam-width. Since the intensity spread over a several millimeter aperture at the lens converges on to a region of the order of micrometers, this varying grid is better suited to obtain the numerical solutions. The resulting equation can be solved by the method of Fourier transforms or by the finite difference method. However, we have used expansion in terms of the closed form basis functions in the radial coordinate combined with the backward Euler method, reducing numerical evaluation of some of the intermediate quantities.

Conclusions about the geometrical profile of the irradiated surface are inferred in literature from the intensity profile of the optical beam, as both should be expected to conform to each other. This provides a reasonable qualitative information[11]. Quantitative description of the surface profile can be determined by considering the interaction mechanism between the optical beam and the material. Recently a procedure was developed from geometrical considerations to determine the structure of a material surface from the knowledge of the intensities and used to calculate the profiles of the surfaces machined with long pulse lasers, where the ablation takes place mainly by melting and evaporating the material. Agreement between the calculated and the observed values was satisfactory except at the peripheries of the craters[14], where some material is accumulated due to fluid flow[15,16]. In cases of short pulse ablation, the amount of melt

is insignificant at fluences close to the threshold, although it increases with increasing intensities[17,18] Thus, the geometrical model is expected to produce reliable profiles of the craters except for deviations at the boundaries of the craters fabricated with high intensities. The numerical scheme based on the geometrical formulation is used in the present article to determine the surface profile from the calculated intensity distribution of the beam.

Calculated structure of the surface is compared with the experimentally obtained crater shape. For a laser beam with pulse-width of 150 femtosecond and the pulse energy of 200 μJ, the self-focusing and plasma effects were found to compensate for each other as long as the radius of the beam at the focal point is larger than about 2 μm. At these intensities no melt was observed and the calculated profile was found to be in good agreement with the experimental, over the entire surface of the crater. The cancellation of these two competing effects was indicated recently by the existence of light filaments in air created with collimated high power short laser pulses[19]. This observation stimulated interest in the studies of the ultra-intense laser pulse propagation in transparent media to exploit the phenomenon for laser fabrication[20-24]. Present results indicate that the experimental parameters can be adjusted to balance the two effects yielding a cleaner surface profile. For more strongly focused beams, the distortion caused by the plasma was found to be significant.

II. NUMERICAL METHOD

Propagation of an optical beam through a dielectric medium is described by the following non-linear Schrodinger equation[11,12]:

$$\frac{\partial A}{\partial z} - \frac{i}{2k}\nabla^2 A = i\left[n_2 kI - \frac{2\pi e^2 N_e(I)}{k m_e c^2} \right] A = i\hat{V}(I)\, A, \qquad (1)$$

satisfied by slowly varying amplitude function A, with intensity $I = |A|^2$. Here ∇^2 denotes the Laplacian in the plane perpendicular to the axis of the beam. Since the effect of air on the value of the wave number $k = (2\pi/\lambda)$ is insignificant, it will be neglected. Self-focusing is described by the first term on the right side in terms of the Kerr coefficient n_2, and the second term describes the effect of plasma in terms of the electron charge e, electron mass m_e and the speed of light c in the gas. Free electron density N_e induced by the laser pulse by field ionization is determined by the rate equation:

$$\frac{\partial N_e(I(\tau))}{\partial \tau} = N_0 R_{ion}(I(\tau)), \tag{2}$$

where N_0 is the number density of the neutral air molecules, R_{ion} is the ionization rate and $\tau = (z - t/c)$ is the retarded time. For propagation in vacuum, the right side in Eq. (1) drops out, yielding the paraxial Helmholtz equation,

$$\frac{\partial A_0}{\partial z} - \frac{i}{2k} \nabla^2 A_0 = 0. \tag{3}$$

Physical solution of Eq. (3) is uniquely determined from its value at one point along the beam axis, usually taken to be the lens location, and the general solution, which is available in closed form[13]. A spacially Gaussian beam after passing through a thin lens remains Gaussian with different characterizing parameters. The lens alters only the phase of the incoming beam with consequent change in its curvature. Curvature of the beam on one side of the lens is determined by its value on the other side and the focal length[13]. Parameters characterizing the

beam on both sides are determined by the curvature on either side of the lens and the beam-width at its location as indicated in Appendix.

The solution $A_0(\xi,\rho,\tau)$ of Eq. (3), after passing through a lens with focal length f satisfying the appropriate conditions at its location, is given by

$$A_0(\xi,\vec{\rho},\tau) \;=\; \kappa(\tau)\,\sqrt{(1+\bar{\xi}^2)/(1+\xi^2)}\,\exp\left[-\frac{\rho^2}{(1+\xi^2)}+i\frac{\rho^2\xi}{(1+\xi^2)}-i\tan^{-1}(\xi)\right]. \qquad (4)$$

Here $\vec{\rho}=(\vec{r}/w_{0f})=\vec{r}\sqrt{\pi/(\lambda z_{0f})}$, where w_{of}, z_{of} and $\vec{r}$ denote the beam-width at the focal point, the corresponding Rayleigh range and the point in the transverse plane, respectively, $\xi(z)=(z-\bar{z}-f)/z_{0f}$ where z is the reference point along the beam axis with the location of lens denoted by $\bar{z}$. The solution given by Eq. (4) is normalized such that the intensity at the lens $|A_0(\bar{\xi},0,\tau(\bar{z}))|^2=|\kappa(\tau(\bar{z}))|^2$.

In terms of these variables, Eq. (1) is expressed as

$$\frac{\partial A}{\partial \xi} - \frac{i}{4}\,\nabla^2_{\vec{\rho}}A \;=\; iV(I)A, \qquad (5)$$

where $V(I)=z_{of}\hat{V}(I)$. At the lens, $A(\bar{\xi},\rho,\tau(\bar{z}))=A_0(\bar{\xi},\rho,\tau(\bar{z}))$. With the above normalization, the intensity $I=I_0\,|A|^2$, where I_0 is the peak input intensity determined by the pulse energy.

Expressing the solution as $A = A_0 A'$ yields the following equation for A':

$$\frac{\partial A'}{\partial \xi} + \frac{(\xi + i)}{(1+\xi^2)} \vec{\rho} \bullet (\nabla_{\vec{\rho}} A') - \frac{i}{4} \nabla^2_{\vec{\rho}} A' - iV(I)A' = 0, \qquad (6)$$

with $A'(\bar{\xi}, \rho, \tau(\bar{z})) = 1$. For convenience, we assume radial symmetry. The following manipulations can be adjusted for the general case in a straightforward manner.

The hyperbolic operator

$$O_h = \left[\frac{\partial}{\partial \xi} + \frac{\xi}{(1+\xi^2)} \rho \frac{\partial}{\partial \rho} \right]$$

can be converted to a complete derivative along the characteristic curve defined by

$$\rho(\xi) = \rho(\bar{\xi}) \sqrt{(1+\xi^2)/(1+\bar{\xi}^2)}$$

and thus, the solution of $O_h\, u(\xi, \rho) = \upsilon(\xi, \rho)$ can be obtained by integration along the curve together with the knowledge of $u(\bar{\xi}, \rho(\bar{\xi}))$, yielding[25],

$$u(\xi, \rho(\xi)) = u(\bar{\xi}, \rho(\bar{\xi})) + \int_{\bar{\xi}}^{\xi} d\eta\, \upsilon\left(\eta, \rho(\bar{\xi}) \sqrt{(1+\eta^2)/(1+\bar{\xi}^2)}\right).$$

The procedure is equivalent to a variable change from $(\xi,\ \rho)$ to

$$(\hat{\xi},\ \hat{\rho}) = \left(\xi,\ \rho\sqrt{(1+\bar{\xi}^2)/(1+\xi^2)}\right)$$

in the differential equation $O_h\, u(\xi,\rho) = \upsilon(\xi,\rho)$. In any case, Eq. (6) is thus reduced to

$$\frac{\partial A'}{\partial \xi} + \frac{i}{(1+\xi^2)}\rho\frac{\partial A'}{\partial \rho} - \frac{i}{4}\left[\frac{\partial^2}{\partial \rho^2} + \frac{1}{\rho}\frac{\partial}{\partial \rho}\right]A' - iV(I)A' = 0 \qquad (7)$$

with the variable ρ depending on ξ as defined by the characteristic curve.

Eq. (7) can be solved by the finite difference method. The solution along ξ can be advanced along an arbitrary mesh, as long as the mesh with respect to ρ conforms to the characteristic curve. The mesh $\{\rho_n(\bar{\xi})\}$ at $\bar{\xi}$ can be arbitrarily selected. At other values of ξ, it is given by $\left\{\rho_n(\bar{\xi})\sqrt{(1+\xi^2)/(1+\bar{\xi}^2)}\right\}$.

While Eq. (7) can be solved by the finite difference scheme, it is not suitable for the applications of the methods, which require a rapid decay of the initial value with respect to ρ, such as the Fourier transform and the expansion in terms of the basis functions. This can be corrected by expressing $A' = (1+B)$, yielding the following inhomogeneous equation in B:

$$\frac{\partial B}{\partial \xi} + \frac{i}{(1+\xi^2)}\rho\frac{\partial B}{\partial \rho} - \frac{i}{4}\left[\frac{\partial^2}{\partial \rho^2} + \frac{1}{\rho}\frac{\partial}{\partial \rho}\right]B - iV(I)B = iV(I) \qquad (8)$$

with $B(\bar{\xi}, \rho(\bar{\xi}), \tau(\bar{z})) = 0$. It is further convenient to change variable from ξ to $\theta = \tan^{-1}(\xi)$, reducing Eq. (8) to

$$\frac{\partial B}{\partial \theta} + iL\,B = iW, \tag{9}$$

where $W = (1+\xi^2)V(I)$ and the operator L is defined by

$$L\,B = \rho\frac{\partial B}{\partial \rho} - (1+\xi^2)\left\{\frac{1}{4}\left[\frac{\partial^2}{\partial \rho^2} + \frac{1}{\rho}\frac{\partial}{\partial \rho}\right] + V(I)\right\} B.$$

The advantage in reducing Eq. (1) to solving Eq. (9) is in isolating the effects of the perturbing terms and in obtaining a suitable grid structure for the radial coordinate. Numerical solutions of Eq. (9) can be obtained by a variety of methods, including the finite difference and the transform methods. However, the use of transforms based on continuous variables is not necessary. It is sufficient to use a discrete basis in the underlying Hilbert space[26]. We have used the method of expansion in terms of basis functions combined with a hybrid Euler method, described below.

The solution B can be expanded in terms of a suitable basis, i.e.,

$$B(\theta, \rho) = \sum_{n=0}^{\infty} \alpha_n(\theta)\,\varphi_n(\rho). \tag{10}$$

Since the τ-dependence of the solution is only parametric entering through the initial condition, it is suppressed for convenience. In numerical calculations, the sum in Eq. (10) is truncated at a

finite value N. Substituting for B in Eq. (9) and taking the scalar product with each of the basis functions, reduces it to an ordinary differential equation:

$$\mathbf{N}\frac{\partial\alpha(\theta)}{\partial\theta} + i\,\mathbf{M}\,\alpha(\theta) = i\,\beta(\theta;\alpha(\theta)), \tag{11}$$

where the N-vector $\beta(\theta)$ and $N\times N$ matrices $\mathbf{N}$ and $\mathbf{M}$ are defined by

$$\beta_n(\theta;\alpha(\theta)) = \langle\varphi_n, W\rangle,\ \mathbf{N}_{n,m} = \langle\varphi_n,\varphi_m\rangle \text{ and } \mathbf{M}_{nm} = \langle\varphi_n, L\,\varphi_m\rangle,\ n,m = 0,\ 1,\ \ldots\ N,$$

with $\langle u,\upsilon\rangle$ denoting the scalar product of functions u and υ in the underlying Hilbert space $\mathcal{H}$, and the N-vector $\alpha(\theta)$ is sought.

Although the solution of Eq. (11) can be expressed in terms of the exponentials of the matrices, application of the backward Euler method is more convenient, which is also quite stable. However, since $\beta(\theta)$ depends on $\alpha(\theta)$, application of fully backward Euler method is inconvenient. Eq. (11) is therefore linearized by a partial application of the forward Euler method. In this hybrid scheme, with $\alpha(\theta)$ known, $\alpha(\theta+d\theta)$ is determined by solving the matrix equation,

$$\left[\mathbf{N} + i\,\mathbf{M}\,d\theta\right]\alpha(\theta+d\theta) = \left[-\mathbf{N}\alpha(\theta) + i\,\beta(\theta,\alpha(\theta))\,d\theta\right]. \tag{12}$$

This determines $\alpha(\theta)$ for all values of θ starting with its value at $\theta=\overline{\theta}=\tan^{-1}(\overline{\xi})$, which is equal to zero.

In view of the radial symmetry, $\mathcal{H}$ can be taken to be a space of symmetric functions of ρ satisfying the requirement of square-integrability with respect to a weight. The basis defined by

$$\varphi_n(\rho) = \left(\frac{\rho}{\rho_{\max}(\theta)}\right)^{2n} \exp\left[-4(\rho/\rho_{\max}(\theta))^2\right]$$

is quite adequate to approximate B, in view of its decay properties. Thus, $\mathcal{H}$ can be taken to be the closure of the span of $\{\varphi_n\}$, which forms a Hilbert space with respect to the scalar product defined by

$$\langle u,v\rangle = \int_0^\infty d\rho\, u(\rho)\, v(\rho) \exp\left[-4(\rho/\rho_{\max}(\theta))^2\right].$$

Constant multiplier in the exponential functions was selected to ensure that $\varphi_n(\rho_{\max})$ is sufficiently small without $\varphi_n(\rho)$ being too small where the solution value is appreciable. However, the solution scheme is not strongly dependent on its value. An advantage of this set is that some of the integrals needed to evaluate the matrix elements can be carried out exactly. The value of $\rho_{\max}(\bar{\theta})$ can be judiciously selected which determines $\rho_{\max}(\theta)$ as it lies on the characteristic curve passing through $\rho_{\max}(\bar{\theta})$. The θ-dependence of the radial mesh is used also in the numerical integrals encountered. In other respects, ρ can be treated as an independent parameter. Alternatively, the above equations can be expressed in terms of the independent parameters ξ and $\hat{\rho}(\bar{\xi})$.

The amplitude $A(\xi,\rho,\tau)$ calculated as described above, determines the intensity $I(\xi,\rho,\tau)$. The intensity distribution can be used to calculate the profile of the processed surface by solving the equation[14]

$$\frac{\partial z(\rho)}{\partial \tau} = -\frac{a_0\, I(\xi,\rho,\tau)}{E_H}\left[1+\left(\frac{\partial z(\rho)}{\partial \rho}\right)^2\right]^{-1/2}, \tag{13}$$

where $z(\rho)$ is the vertical coordinate of the surface at the radial position ρ, a_0 is the absorption coefficient of the material, E_H is the energy needed to remove unit volume of the material, which is determined by independent considerations of the laser-material interaction. Eq. (13) is conveniently solved by the forward Euler method, which has been found to yield quite accurate values.[14]

III. RESULTS AND DISCUSSION

Calculated surface profile was compared with the surface of the craters fabricated during the interaction of short-pulsed lasers with thin sheets of copper. The laser system used was a Clark-MXR CPA 2010 femtosecond laser, which consists of a 35 MHz SErF fiber oscillator and a chirped-pulse-amplification, Ti: Sapphire regenerative amplifier, which deliveres 150 fs single pulses with wavelength centered at 775 nm with average power of 1 W corresponding to the maximum pulse energy of 1 mJ, at pulse repetition rate of 1 kHz. A set of ND filters was used to control the pulse energy. The laser beam was collimated with a beam expander and focused with a chromatic objective (CVI Laser Co.) with NA = 0.23 and $f = 21\ mm$. The copper foil sample with a thickness of 70 μm was mounted on a motion stage having a positioning

accuracy within 1 μm. In order to ensure that each laser ablated crater on the copper surface be produced by a single pulse, the motion system translated at a speed of 750 $mm/\min$, while the laser fired at a pulse repetition rate of 500 Hz, separating the craters by 25 μm. For various experimental considerations, experiments were conducted at the pulse energy of 200 μJ. The depth at various locations of each crater was measured by an optical interferometric WYCO surface profiler (model NT-2000), which provides a 1 nm resolution in its vertical-scanning interferometry mode.

A picture of the typical craters and corresponding depth profiles in two perpendicular directions are shown in Figure 1. The craters produced were not identical to each other due to noticeable random variations. The observations selected are deemed to represent the observed profiles adequately. For comparison with the theoretical values calculated for a radially symmetric system, the depths along X and Y - axes were averaged to obtain the profile with respect to the radial distances and measured data was also averaged over a number of measurements to minimize the effects of the statistical variations. Since the representative experimental profile is obtained by averaging the X and Y profiles, it is radially symmetric and due to cancellations of the statistical variations, the averaged profile is smoother than the individual craters.

In conformity with the laser used, the profile of the input laser beam with respect to time was also assumed to be Gaussian, given by Eq. (4) with

$$\kappa(\tau(\bar{z})) = \kappa(t) = I_0 \exp[-\bar{\kappa}(t/\tau_p)^2],$$

where τ_p is the pulse-width and the laser specific parameter $\bar{\kappa} = 4 \log(2)$. Input peak power

I_0 is calculated from the pulse energy E_{pulse} given by

$$E_{pulse} = I_0 \int_{-\infty}^{\infty} dt \int_{-\infty}^{\infty} dx \int_{-\infty}^{\infty} dy \; \exp[-2(x^2 + y^2)/(D_B/2)^2 - \bar{\kappa}(t/\tau_P)^2] = \frac{1}{8}\pi D_B^2 I_0 \tau_P \sqrt{\frac{\pi}{\bar{\kappa}}} \quad , \tag{14}$$

where the input beam diameter $D_B = 2\,(1 + \bar{\xi}^2)$.

Although the effects of melting and vaporization on the ablation process with short-pulsed lasers are insignificant, the energy E_H in Eq. (13) is still given quite accurately by its amount needed to melt and evaporate unit volume of the metal.[14] The ionization rate $R_{ion}(I)$ needed to calculate $N_e(I)$ from Eq. (2) was determined from the experimental values for N_2 and O_2, assuming their concentrations to be 80% and 20%, respectively in the atmosphere. The values for N_2 and O_2 were calculated by a polynomial fit to their experimentally measured values in the required energy range[27] In Eq. (12), less than ten basis functions were found to be sufficient to produce reliable results. The results changed little for more than five basis functions.

Theoretical predictions and the averaged experimental values of the depth with respect to the radial distance with origin at the intersection of the axis of the beam and the horizontal surface of the sheet are displayed in Figure 2, for a spot diameter of about 10 μm. The calculated and the measured values are in close agreement for this spot size. Figure 3 shows the calculated intensity profile of the optical beam normalized in units of the peak input intensity, for the waist radius at the focal point equal to 1 μm. Experimental values were unavailable for

the correspondingly small spot size. However, this profile resembles other calculations of this type, which compare well with the experimental observations available in literature. [9,12] Also, at higher intensities, additional phenomena must be taken into account in modeling the laser-material interaction and to determine the surface profile adequately, which is beyond the scope of the present article.

It is clear from Figure 2, that with a spot size of 10 μm the Gaussian profile of the optical beam propagating through air remains relatively undistorted in shape indicating a significant cancellation of the self-focusing and plasma effects at medium intensities. This behavior was found to persist up to the waist radius of about 2 μm. Such cancellations have been noticed in the observations of long filaments of light in air created with collimated short pulse optical beams.[19] Studies aimed at generating shot columns of plasma in converging beams used for laser machining have been conducted recently.[20-24] Existence of a region in a beam with relatively undistorted profile can be exploited to fabricate cleaner surfaces. Present results indicate that a desirable beam profile can be created at intensities close to the threshold. Since the melt at such intensities is negligible[17,19], the associated distortions at the boundaries of the craters, are also minimized. As indicated by the results of Figure 3, the distortions caused by plasma are significant at higher intensities.

IV. CONCLUDING REMARKS

A numerical scheme is developed to determine the intensity profile of an optical beam propagating through a dielectric medium such as air. The scheme is perturbative in nature as it isolates the effect of the medium on the profile in vacuum, which is exactly available. Since the self-focusing and plasma effects caused by a medium tend to cancel each other over a wide

range of intensities, the approach is pre-eminently suitable. Also, the mesh suggested by the characteristics of the beam in vacuum is better suited for accurate and efficient calculations of the intensity distribution at a desired location. Further, it is indicated that instead of continuous transforms, a finite basis set is sufficient to assure convergence. The scheme is coupled with a geometrical scheme to calculate the surface profile of the laser-ablated craters.

The scheme is verified by comparing the calculated values with the average surface profile of the experimentally ablated craters with single pulse of a short-pulsed high intensity laser. Experimental values were available only for lower intensities and found to be in close agreement. At higher intensities, where experimental surface profiles are not available, the calculated beam profile agrees qualitatively with other calculations, which are in qualitative agreement with the fabricated surface profiles, available in literature.

The results indicate that for lower intensities, the self-focusing caused by the medium and the impact of the plasma generated by the high intensity laser beam, tend to cancel each other. Such intensities can be obtained by adjusting the experimentally controllable parameters to produce a spot size with corresponding intensities in a desirable range yielding cleaner machined surfaces. For a smaller spot size corresponding to higher intensities, the plasma was found to distort the intensity distribution in the beam.

Acknowledgements

Thanks are due to M. Islam, Director, Production Technology Research, IMTI, for his continued support.

References

1. K. Hirao, K. Mirua, J. Non-Cryst. Solids, **239**, 91 (1998).
2. L. Sudrie, M.Franco, B. Prade, A. Mysyrowicz, Opt. Commun., **191**, 333 (2001).
3. A. Marcinkevicius, S. Juodkazis, and J. Nishii, Opt. Lett., **26**, 277(2001).
4. K. Venkatakrishnan, B. Tan, P. Stanley, L. E. N. Lim, B. K. A. Ngol, Optical Engineering, **41**, 1441(2002).
5. P. Pronko, S. Dutta, J. Squier, Opt. Commun. **114**, 106 (1995).
6. S. Nolte, C. Momma, G.Kamlage, A. Ostendorf, C. Fallnich, F. von Alvensleben, H. Welling, Appl. Phys. A, **68**, 563 (1999 Physics A, **68**, 563 (1999).
7. M. Meunier, B. Fisette, A. Houle, A. V. Kabashin, S. V. Broude, P. Miller, SPIE USE, **6**, 4978 (2003).
8. C. Momma, S. Nolte, G.Kamlage, F. von Almensleben, A. Tunnermann, Appl. Phys. A, **67**, 517 (1998).
9. J. Sun and J.P. Longtin, J. Appl. Phys. **89**, 8219 (2001).
10. C. Li and S. Nikumb, Applied Optics, **42**, 2383 (2003).
11. A. Chiron, B. Lamourous, R. Lange, J. F. Ripoche, M. Franco, B. Prade, G. Bonnaud, G. Riazuelo, and A. Mysyrowicz, Eur. Phys. J. D, **6**, 383 (1999).
12. S.L. Chin, N. Akozbek, A. Proulx, S. Petit, and C.M. Bowden, Opt. Commun. **188**, 181 (2001).
13. B. A. Saleh and M. C. Teich, Fundamentals of Photonics (John Wiley & Sons, Inc., New York, 1991) Ch. 3.
14. S. R. Vatsya, E. V. Bordatchev and S. K. Nikumb, J. Appl. Phys. **93**, 9753 (2003).
15. T. Schwarz-Selinger, D. G. Cahill, S. C. Chen, S. J. Moon and C. P. Grigoropoulos, Phys. Rev. B **64**, 15 5323 (2001).
16. S. R. Vatsya and S. K. Nikumb, Phys. Rev. B **68**, 03 5410 (2003).
17. N. N. Nedialkov, S. E. Emamova. P. A. Atanasov, G. Heusel, D. Breitling, A. Ruf, H. Hügel, F. Dausinger and P. Berger, Thin Solid Films, **453-454**, 496 (2004).

18. S. S. Klimentov, T. V. Kononenko, P. A. Pivovarov, S. V. Garnov, V. I. Konov, A. M. Prokhorov, D. Breitling and F. Dausinger, Quantum Electron., **31**, 378 (2001).
19. A. Braun, G. Korn, X. Liu, D. Du, J. Squier, and G. Mourou, Opt. Lett., **20**, 73 (1995).
20. A. Talebpour, M. A. Fattah, and S. L. Chin, Opt. Commun., **183**, 479 (2000).
21. J. Schwarz, P. Rambo, J. C. Diels, M. Kolesik, E. M. Wright, J. V. Moloney, Opt. Commun., **180**, 383 (2000).
22. J. Kasparian, R. Sauerbrey, S. L. Chin, Appl. Phys. B **71**, 877 (2000).
23. B. Tzortzakis, L. Berge, A. Couairon, M. Franco, B. Prade, and A. Mysyrowicz, Phys. Rev. Lett., **86**, 5470 (2001).
24. A. Couairon and L. Berge, Phys. Rev. Lett., **88**, 135003-1 (2002).
25. R. Courant and D. Hilbert, Methods of Mathematical Physics, Vol. II, Third Printing, (Interscience Publishers, Inc., New York, 1961) Ch. V, Sec. 2.
26. S. R. Singh, J. Math. Phys., **18**, 1466 (1977), Theorem 1.
27. A. Talebpour, J. Yang and S. L. Chin, Opt. Commun. **163**, 29 (1999).

Appendix

Consider a Gaussian beam passing through a thin convex lens of the aperture radius w_l and focal length f. Here the parameters characterizing the beam on both sides of the lens are calculated in terms of these input parameters from the standard relations.[13]

Let w_{0f} and z_{0f} be the beam-width and the Rayleigh range at the focal point. Taking the focal point as the reference point where the curvature is zero, the beam-width w_l on both sides of the lens is given by

$$w_l = w_{0f}\left[1 + \left(\frac{f}{z_{0f}}\right)^2\right]^{1/2}, \tag{A-1}$$

with $w_{0f}^2 = (\lambda z_{0f})/\pi$ where λ is the wavelength yielding

$$z_{0f} = \left(\frac{\pi w_l^2}{2\lambda}\right) - \sqrt{\left(\frac{\pi w_l^2}{2\lambda}\right)^2 - f^2}, \tag{A-2}$$

The radii of curvature R_f and R_l on the side of the focal point and the input beam, respectively, are given by $(1/R_f) = -f/(z_{0f}^2 + f^2)$, and $(1/R_l) = [(1/f) + (1/R_f)]$. The beam-width at the narrowest point of the input beam, which is taken to be the origin of the axis along the axis of the beam, is given by

$$w_0 = w_l\left[1+\left(\frac{\pi w_l^2}{\lambda R_l}\right)^2\right]^{-1/2}, \qquad \text{(A-3)}$$

with the corresponding Rayleigh range $z_0 = (\pi w_0^2)/\lambda$. This determines the location $\overline{z}$ of the lens with respect to this origin to be

$$\overline{z} = R_l\left[1+\left(\frac{\lambda R_l}{\pi w_l^2}\right)^2\right]^{-1}. \qquad \text{(A-4)}$$

Figure captions

Figure 1. Typical laser machined craters and the corresponding profiles of the ablated surface with laser of pulse-width = 150 fs, wavelength = 775 nm, and pulse energy = 200 μJ.

Figure 2. Comparison of theoretical (solid line) and averaged experimental (circles) profile of the surface machined in air with laser of pulse-width = 150 fs, wavelength = 775 nm, pulse energy = 200 μJ and spot diameter at focal point $\simeq$ 10 μm.

Figure 3. Calculated intensity profile of the optical beam propagating in air with laser of pulse-width = 150 fs, wavelength = 775 nm, pulse energy = 200 μJ and spot diameter at the focal point $\simeq$ 2 μm.

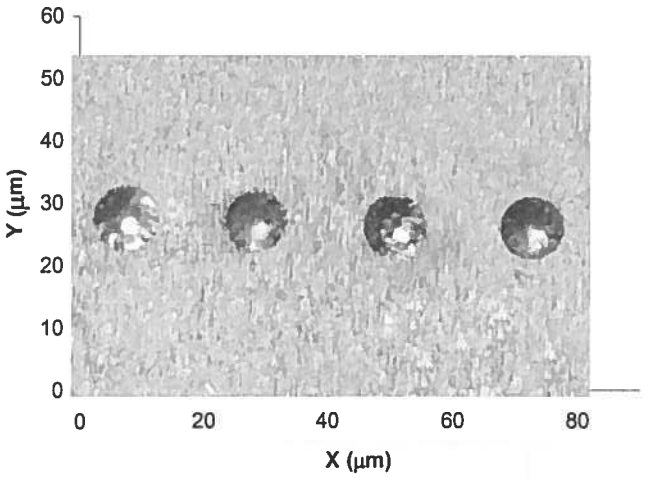

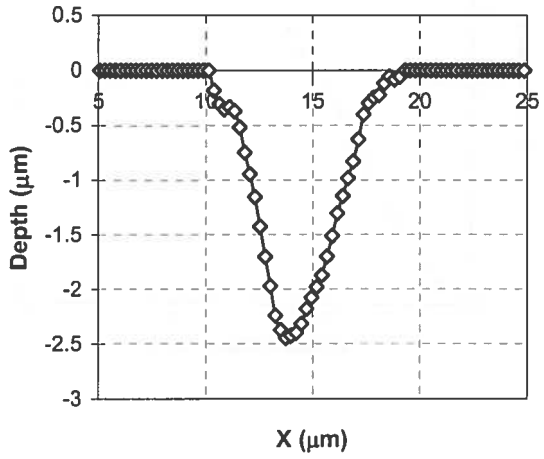

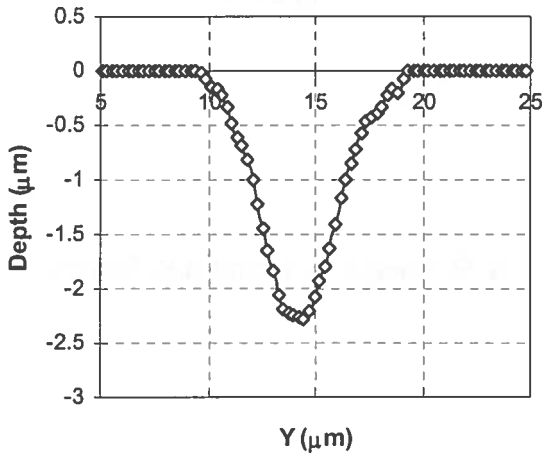

Figure 1. S. R. Vatsya, C. Li and S.K. Nikumb

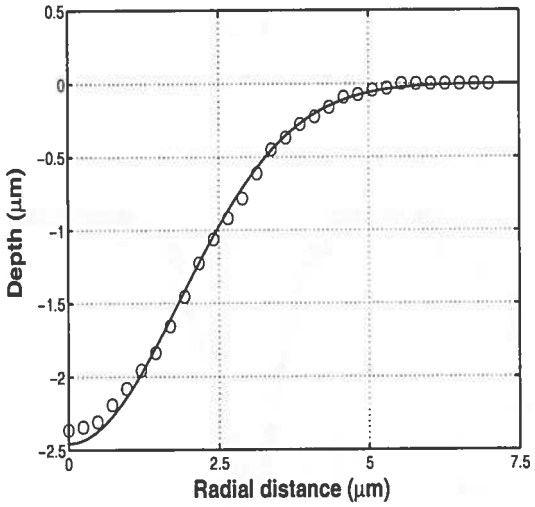

Figure 2.

S. R. Vatsya, C. Li and S.K. Nikumb

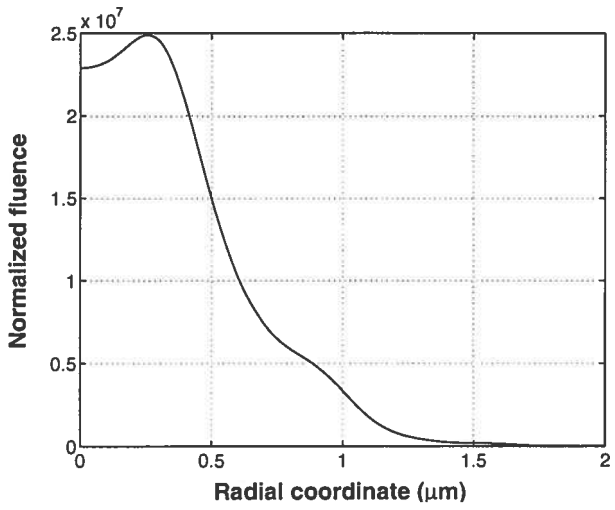

Figure 3.

S. R. Vatsya, C. Li and S.K. Nikumb